

# Resonances in rotationally inelastic scattering of OH( $X^2\Pi$ ) with helium and neon

Koos B. Gubbels,<sup>1,2,\*</sup> Qianli Ma,<sup>3</sup> Millard H. Alexander,<sup>4</sup> Paul J. Dagdigian,<sup>3</sup> Dick Tanis,<sup>2</sup>  
Gerrit C. Groenenboom,<sup>2</sup> Ad van der Avoird,<sup>2</sup> and Sebastiaan Y. T. van de Meerakker<sup>2</sup>

<sup>1</sup>*Fritz-Haber-Institut der Max-Planck-Gesellschaft, Faradayweg 4-6, D-14195 Berlin, Germany*

<sup>2</sup>*Radboud University Nijmegen, Institute for Molecules and Materials, Heyendaalseweg 135, 6525 AJ Nijmegen, The Netherlands*

<sup>3</sup>*Department of Chemistry, The Johns Hopkins University, Baltimore, Maryland 21218-2685, USA*

<sup>4</sup>*Department of Chemistry and Biochemistry and Institute for Physical Science and Technology, University of Maryland, College Park, MD 20742-2021, USA*

(Dated: January 17, 2012)

We present detailed calculations on resonances in rotationally and spin-orbit inelastic scattering of OH ( $X^2\Pi$ ,  $j = 3/2$ ,  $F_1$ ,  $f$ ) radicals with He and Ne atoms. We calculate new *ab initio* potential energy surfaces for OH-He, and the cross sections derived from these surfaces compare favorably with the recent crossed beam scattering experiment of Kirste *et al.* [Phys. Rev. A **82**, 042717 (2010)]. We identify both shape and Feshbach resonances in the integral and differential state-to-state scattering cross sections, and we discuss the prospects for experimentally observing scattering resonances using Stark decelerated beams of OH radicals.

## I. INTRODUCTION

Measurements of state-to-state cross sections provide important tests of the reliability of computed potential energy surfaces (PES's) describing the interaction of atoms and molecules [1]. Cross sections for collision-induced rotational transitions are sensitive to the anisotropy of the PES. Since non-bonding interactions are relatively weak, the magnitudes of the cross sections are mostly sensitive to the repulsive part of the PES, except at very low collision energies. An alternative, spectroscopic approach to gaining information on PES's is the determination of the energies of the bound levels of van der Waals complexes of the collision partners [2, 3]. The energies of the bound levels are mainly sensitive to the attractive part of the PES's. As we go up higher in the manifold of these weakly bound levels, the energies of these levels eventually become higher than the dissociation energy of the complex, and such levels are quasi-bound. These quasi-bound levels are often described as resonances and can be thought of as a distortion of the continuum in the collision energy dependence of state-to-state cross sections [4]. In inelastic scattering, resonances are called shape or orbiting resonances when the quasi-bound levels involve monomer levels that are the same as in the initial or final level of the collision-induced transition, or Feshbach resonances when they involve different monomer states [1, 4]. Due to their sensitivity to the PES, resonances can reveal important information on the PES [5, 6]. So far, however, resonant structures in scattering cross sections have been experimentally observed only in exceptional cases [7–10].

The crossed molecular beam technique has been an extremely useful tool for the determination of state-to-

state cross sections, both integral and differential, as well as their dependence upon the collision energy [11]. The recently developed Stark deceleration technique, taking advantage of the interaction of polar molecules with time-varying electric fields, has allowed continuous tuning of the beam velocity [12]. This has facilitated measurements of the collision energy dependence of state-to-state integral cross sections down to energies of  $70\text{ cm}^{-1}$  [13]. Moreover, the velocity spread in such decelerated beams is much smaller than in conventional molecular beams. Thus far, an energy resolution of  $\geq 13\text{ cm}^{-1}$  has been achieved for collisions of OH radicals with rare gas atoms [13–15]. This resolution is mainly limited by the velocity and angular spread of the atomic collision partner, and is too low to experimentally resolve scattering resonances. A recent study has shown that the energy resolution can be improved significantly by an appropriate choice of the beam velocities and interaction angle [16]. When these measures are put into practice in the laboratory, collision energy resolutions can be obtained that may enable the observation of scattering resonances.

Atom-molecule collisions are the simplest type of collision process in which rotationally inelastic transitions can be observed. Early calculations [17, 18] on rotationally inelastic scattering of  $\text{N}_2$  molecules with He atoms have shown that resonances occur at low collision energies, but the experimental verification of these predictions was not yet possible. Collisions of OH( $X^2\Pi$ ) with rare gases have emerged as paradigms of scattering of an open-shell molecule with an atom [13, 15, 19–24]. The OH-rare gas systems are good candidates for the observation and analysis of resonances in rotationally inelastic collisions because the collision energy can be reduced by Stark deceleration of the OH beam. Since OH( $X^2\Pi$ ) is an open-shell molecule with orbital degeneracy, the collision dynamics is governed by two PES's,[25] and interesting multi-state dynamics can occur. Of particular interest for the study of resonances are the OH-He and

---

\*Electronic address: K.B.Gubbels@science.ru.nl

OH-Ne systems, since the dissociation energies of these systems are smaller than the rotational level spacings of the OH radical. The resonance features associated with the various rotational levels are therefore well separated. The shallow van der Waals wells support only one or two stretch vibrational levels [26], resulting in a rather simple, yet interesting, analysis of the resonances. Shape resonances in OH-He collisions were previously analyzed by Dagdigian and Alexander[24] in a study of elastic depolarization. Bound states of the OH-He complex have been investigated spectroscopically by Han and Heaven, who identified complex features as scattering resonances in OH(A)-He [27].

Here, we present a detailed and precise study of scattering resonances in the OH-He and OH-Ne systems, in order to develop insight into the nature and strength of the resonances and to assist in the experimental search for such scattering resonances. For the OH-He system, we have calculated new three dimensional potential energy surfaces. The collision energy dependence of the relative state-to-state integral scattering cross sections that are derived from these potentials compares more favorably with recent experiments [15] than the results from previous calculations. For the correct assessment of the resonances, the calculations are performed on a very fine grid of collision energies, and particular care is taken to converge the calculations to avoid numerical artifacts to be interpreted as resonant structures [28]. We characterize the resonances with various techniques, including the adiabatic bender model [29, 30] and collision lifetime analysis [31]. We investigate how the differential cross section for several transitions changes as the collision energy is scanned through the resonances, and observe dramatic effects.

This paper is organized as follows: The details of the scattering calculations are briefly presented in Section II. In Section III we describe the new three-dimensional (3D) PES's that are developed for OH-He. Section IV describes our calculations on the state-to-state scattering cross sections in OH-He collisions. A detailed analysis of shape and Feshbach resonances is given. Section V presents similar results for the OH-Ne system. A discussion of the prospects for observing these resonances in crossed beam experiments using a Stark decelerator, by either recording the integral or the differential cross sections, follows in Sec. VI.

## II. SCATTERING CALCULATIONS

The theory of scattering between a molecule in a  ${}^2\Pi$  electronic state and a structureless atom is well established [25]. The interaction can be described by two PES's corresponding to states of  $A'$  and  $A''$  symmetries. For OH-He, we have constructed new PES's, which are explained in Sect. III, while for OH-Ne, we used the PES's by Sumiyoshi et al. [32]. Close-coupling calculations were performed both with the HIBRIDON suite of

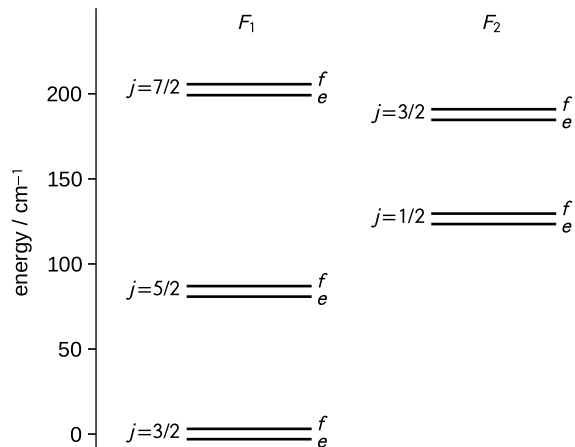


FIG. 1: Energies of the lower rotational levels of OH( $X^2\Pi$ ). The  $\Lambda$ -doublet splitting is exaggerated for clarity. The initial level for all scattering calculations is the  $j = 3/2, F_1, f$  level.

programs [33], and with a second independent scattering program for open-shell diatom-atom scattering described in Ref. 34. Care was taken to independently check the results with the two scattering programs and to converge the cross sections. For OH-He the maximum total angular momentum was  $J = 100.5 - 140.5$ , depending on the collision energy, and the channel basis consisted of all rotational levels of OH with  $j \leq 6.5$ , while for OH-Ne the channel basis consisted of all rotational levels with  $j \leq 7.5$ . In this paper, we calculate cross sections from fully converged close-coupling calculations in order to study resonances in inelastic collisions between low-lying rotational states of the OH radical. For reference, the energies of the lower rotational levels of OH( $X^2\Pi$ ) are displayed graphically in Fig. 1.

## III. 3D OH-HELIUM POTENTIAL

A crucial role in the scattering calculations is played by the interaction potential. In Ref. 34 a detailed experimental and theoretical study of inelastic scattering between OH radicals and the rare gas atoms He, Ne, Ar, Kr and Xe was performed. The theoretical results in that study were shown to be in excellent agreement with experimentally measured inelastic cross sections. The agreement between theory and experiment was, although still very good, the worst for the OH-He system. It was believed that this was due to the quality of the PES, since for the OH-He system a smaller basis set was used in the calculations than for the other systems. For this reason, we construct here a new potential for the OH-He system. We note that in Ref. 34 the experimental resolution was unfortunately not yet high enough to observe resonances.

In trying to improve the agreement with the experimental results, we first constructed new 2D PES's for OH-He collisions. This was done by enhancing the ba-

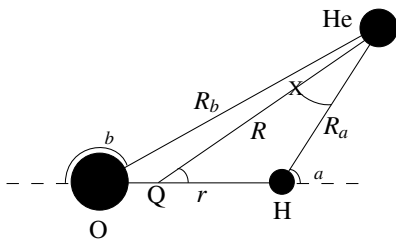


FIG. 2: Illustration of the OH molecule and the He atom containing the relevant coordinates as used in the fitting of the OH-He potential.  $R$  is the length of the vector  $\mathbf{R}$  that connects the He atom and the center-of-mass ( $Q$ ) of the OH molecule, while  $\theta$  is the angle between  $\mathbf{R}$  and the OH bond vector  $\mathbf{r}$  (pointing from  $O$  to  $H$ ) of length  $r$ .  $R_a$  is the length of the vector  $\mathbf{R}_a$  that connects the He atom and the H atom, while  $\theta_a$  is the angle between  $\mathbf{R}_a$  and  $\mathbf{r}$ .  $R_b$  is the length of the vector  $\mathbf{R}_b$  that connects the He atom and the O atom, while  $\theta_b$  is the angle between  $\mathbf{R}_b$  and  $-\mathbf{r}$ . The point  $X$  marks the location of the midbond orbitals.

sis set for the coupled-cluster calculations of the interaction energy from the augmented triple-zeta correlation-consistent basis set (AVTZ) used by Lee et al. [26] to the quintuple-zeta basis set (AV5Z). We computed the interaction energies with the open-shell single and double excitation coupled cluster method with perturbative triples as implemented in the MOLPRO package [35]. The interaction energies were evaluated for 288 geometries on a two-dimensional grid with 12 Gauss-Legendre points in the Jacobi-angle  $\theta$ . The OH bond length was fixed at the vibrationally averaged distance of  $r_0 = 1.8502 a_0$ , whereas Lee et al. used the equilibrium distance  $r_e$ . The relevant geometry is illustrated in Fig. 2. We included midbond orbitals ( $3s, 3p, 2d, 1f, 1g$ ) with the exponents of Ref. 36. These midbond functions were centered on the vector  $\mathbf{R}$  that connects the He atom and the center-of-mass of the OH molecule, at a distance from the helium atom that is half the distance of the helium atom to the nearest atom of the OH molecule. Also the counterpoise correction of Boys and Bernardi was applied [37]. The grid of atom-molecule separations consisted of 18 points ranging from  $R = 3 a_0$  to  $9 a_0$  at short range and 6 points on an approximately logarithmic scale up to  $25 a_0$  at long range.

As mentioned before, two potential energy surfaces belonging to states of  $A'$  and  $A''$  symmetry are involved in the OH-rare-gas atom scattering. The average  $V_s$  and half-difference  $V_d$  of these potentials can be expanded in Racah normalized spherical harmonics  $C_{l,m}$ , namely

$$\begin{aligned} V_s &= \frac{V_{A'} + V_{A''}}{2} = \sum_{l=0}^{l_{\max}} v_{l,0}(R) C_{l,0}(\theta, 0), \\ V_d &= \frac{V_{A''} - V_{A'}}{2} = \sum_{l=2}^{l_{\max}} v_{l,2}(R) C_{l,2}(\theta, 0), \end{aligned} \quad (1)$$

where we included all terms up to  $l_{\max} = 11$ . In the long range ( $R > 10a_0$ ), the expansion coefficients  $v_{l,0}(R)$  were

fitted to inverse powers  $R^{-n}$  with  $n \geq 6$ , namely

$$v_{l,0}^{\text{lr}}(R, \theta) = \sum_{n=n_0(l)}^{11} c_{l,n} \frac{f_n(\beta R)}{R^n}, \quad (2)$$

where we note that the allowed values for  $n$  depend on  $l$  [38]. For example, for  $l = 0$  we have  $n_0(l) = 6$  and only even values of  $n$  are present, while for  $l = 1$  we have  $n_0(l) = 7$  and only odd values of  $n$  are present. From the fitted coefficients we only kept the leading long-range terms for  $l = 0$  to  $l = 4$ . We used the Tang-Toennies damping function [39]

$$f_n(x) = 1 - e^{-x} \sum_{k=0}^n \frac{x^k}{k!} \quad (3)$$

to damp these five long-range terms in the short range with  $\beta = 0.6a_0^{-1}$ . In the short range ( $R < 5.5a_0$ ), the expansion coefficients  $v_{l,0}(R)$  were fitted to an exponential, namely

$$v_l^{\text{sr}}(R) = s_l e^{-\alpha_l R}. \quad (4)$$

The difference between the *ab initio* interaction energies and the analytic long range and short range functions was fitted with a reproducing kernel Hilbert space (RKHS) method [40]. The RKHS parameter  $m$  was chosen such that the RKHS fit would decay faster than the leading long-range term for each  $l$ . The RKHS smoothness parameter was set to 2. For the expansion coefficients of the difference potential,  $v_{l,2}(R)$ , no analytic short range and long range fit was performed, so that everywhere the RKHS method was used. Using the described procedure, we obtained an accurate fit to the *ab initio* points. More details of the fit can be found on EPAPS [41], where we provide a FORTRAN 77 code for the two-dimensional AV5Z potential.

We found that the absolute minimum of the fitted potential is located at  $\theta = 68.7^\circ$ ,  $R = 5.69 a_0$  on the  $A'$  PES, corresponding to an interaction energy of  $V_{A'} = -29.8 \text{ cm}^{-1}$ . The minimum potential energy values for  $\theta = 0^\circ$  and  $\theta = 180^\circ$  were found at  $R = 6.56 a_0$  and  $R = 6.09 a_0$ , giving rise to  $V_{A'/A''} = -27.1 \text{ cm}^{-1}$  and  $V_{A'/A''} = -21.6 \text{ cm}^{-1}$ , respectively. For comparison, we also mention the values obtained by Lee et al. [26], who found that the absolute minimum of their potential was located at  $\theta = 68.6^\circ$ ,  $R = 5.69 a_0$  for  $A'$  symmetry, with an interaction energy of  $V_{A'} = -30.0 \text{ cm}^{-1}$ . The minimum values for  $\theta = 0^\circ$  and  $\theta = 180^\circ$  were found at  $R = 6.54 a_0$  and  $R = 6.09$ , giving rise to  $V_{A'/A''} = -27.1 \text{ cm}^{-1}$  and  $V_{A'/A''} = -21.8 \text{ cm}^{-1}$ , respectively. The two potentials are seen to give very similar results for the local and global minima. Moreover, using the new AV5Z potential for scattering calculations, we found only a very slight improvement in the agreement with the experimental data.

Therefore, we tried to improve the PES further by taking the vibrational motion of the OH radical into account. To this end, we computed the interaction energies of the OH-He system on a three-dimensional grid.

At short and intermediate range we used a step size of  $\Delta R = 0.25 a_0$  for  $3 a_0 \leq R \leq 12.5 a_0$  and  $\Delta r = 0.25 a_0$  for  $0.75 a_0 \leq r \leq 4.5 a_0$ . For the angle  $\theta$  we used an equidistant grid of 16 points including 0 and  $180^\circ$  with a spacing of  $\Delta\theta = 12^\circ$ . At long range we used 4 equidistant points between  $14 \leq R \leq 20$ , while we used a step size of  $\Delta r = 0.5 a_0$  for  $0.75 a_0 \leq r \leq 4.25 a_0$ . The distance  $r = 4.5 a_0$  was also included in the long-range fit. For the angle  $\theta$  we used an equidistant grid of 9 points with a spacing of  $\Delta\theta = 22.5^\circ$ . On this grid we computed the interaction energies with a triple-zeta basis set (AVTZ) and using midbond orbitals with geometry-dependent exponents [42]. Especially for large  $r$  and small  $R$ , the electronic structure calculations did not always converge. Then, we obtained the energy for the corresponding grid point by means of interpolation or extrapolation from neighbouring grid points.

To perform the fit of the sum interaction potential  $V_s$ , we proceed in the following way. We represent the potential as a sum of three terms, namely

$$V_s(R, \theta, r) = V_s^{\text{sr}}(R_a, \theta_a, r) + V_s^{\text{sr}}(R_b, \theta_b, r) + V_s^{\text{lr}}(R, \theta, r), \quad (5)$$

where the different coordinates are defined in Fig. 2. This representation is convenient because the coordinates of the first and second term of Eq. (5) are ideally suited to describe the short-range behavior near the H and O atom, respectively, while the coordinates of the third term are convenient to describe the long-range behavior. The short-range terms are fitted by

$$V_s^{\text{sr}}(R_i, \theta_i, r) = \sum_{l=0}^{l_{\text{max}}^0} e^{-\beta_i R_i} P_l(\cos \theta_i) s_l^{(i)} + \sum_{l=0}^{l_{\text{max}}^i} \sum_{k=0}^{k_{\text{max}}^i} \sum_{n=0}^{n_{\text{max}}^i} R_i^n e^{-\beta_i R_i} P_l(\cos \theta_i) r^k e^{-\alpha_i r^3} s_{lnk}^{(i)}, \quad (6)$$

where  $i = a, b$ , while  $P_l(x)$  are Legendre polynomials corresponding to the functions  $C_{l,0}(\theta, 0)$  of Eq. 1. We used the values  $l_{\text{max}}^0 = 1$ ,  $n_{\text{max}}^a = 3$ ,  $k_{\text{max}}^a = 8$ ,  $l_{\text{max}}^a = 7$ ,  $n_{\text{max}}^b = 3$ ,  $k_{\text{max}}^b = 8$  and  $l_{\text{max}}^b = 5$ . The long range term is fitted by

$$V_s^{\text{lr}}(R, \theta, r) = \sum_{n=6}^{13} \sum_{l=0}^{n-4} \frac{f_n(\beta R)}{R^n} P_l(\cos \theta) c_{nl}(r), \quad (7)$$

where  $f_n$  is the damping function of Eq. (3). Nonzero values of  $c_{nl}$  occur only for even values of  $l+n$ , and then they are given by

$$c_{nl}(r) = c_{nl}^0 + \sum_{k=0}^3 r^k e^{-\alpha_n r^3} c_{nlk}. \quad (8)$$

We use two different values for  $\alpha_n$ , namely  $\alpha_n = \alpha_{\text{I}}$  for  $6 \leq n \leq 9$ , and  $\alpha_n = \alpha_{\text{II}}$  for  $10 \leq n \leq 13$ . For the difference potential  $V_d$  similar fit functions are used, only

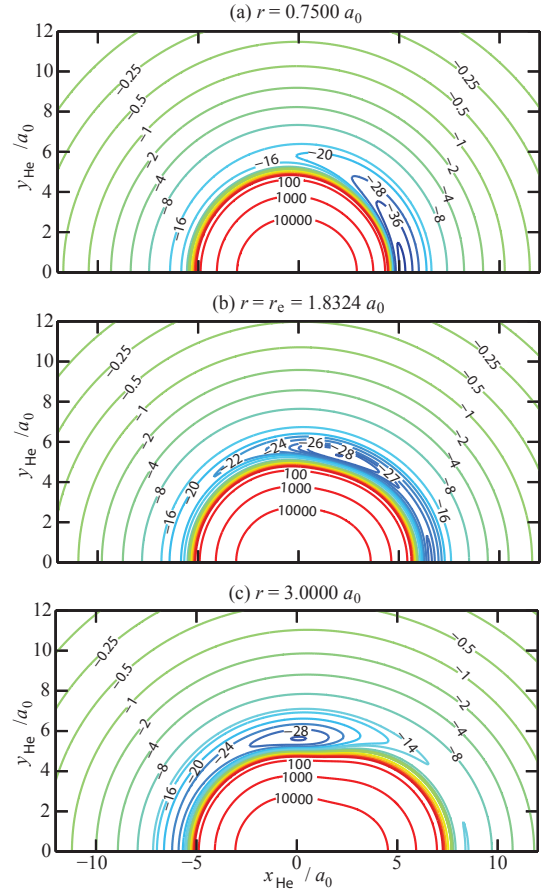


FIG. 3:  $A'$  potential energy surface. The OH radical lies on the horizontal axis, with the center-of-mass of the molecule at the origin. The O atom lies left of the origin, the H atom to the right. For each geometry of the complex, defined by the OH bond length  $r$  and the position  $(x_{\text{He}}, y_{\text{He}})$  of the He atom, the interaction energy is calculated, resulting in contours with the unit of  $\text{cm}^{-1}$ . The three plots differ in the OH bond length, namely in panel a) we have  $r = 0.75 a_0$ , in panel b)  $r = 1.8324 a_0$ , and in panel c)  $r = 3.00 a_0$ .

now the Legendre polynomials  $P_l(x)$  are replaced by associated Legendre functions  $P_l^2(x)$  corresponding to the Racah spherical harmonics  $C_{l,2}(\theta, 0)$  of Eq. 1, so that all sums start with  $l = 2$ . Moreover, we use  $l_{\text{max}}^0 = 2$ ,  $n_{\text{max}}^a = 5$ ,  $k_{\text{max}}^a = 5$ ,  $l_{\text{max}}^a = 6$ ,  $n_{\text{max}}^b = 5$ ,  $k_{\text{max}}^b = 4$  and  $l_{\text{max}}^b = 6$ . The linear and the nonlinear fit parameters were determined by minimizing a weighted least-squares error.

By evaluating the analytic representation of the potential on the *ab initio* grid, we were able to compare the fitted energy values with the *ab initio* values. We found that we only obtained a reliable fit for OH bond lengths  $r \leq 3 a_0$ . At smaller values of  $R$  the largest relative error of an analytic value compared to an *ab initio* value for  $r \leq 3 a_0$  was 6.67% for the sum potential and 1.10% for the difference potential. At large  $R$ , again considering only  $r \leq 3 a_0$ , the largest relative error was 3.23 % for



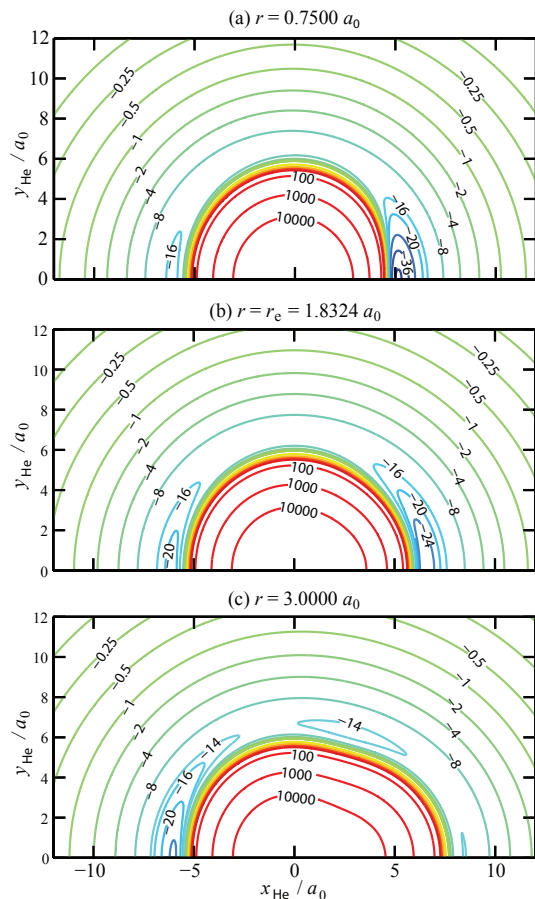


FIG. 4: Similar to Fig. 3, but showing the  $A''$  potential energy surface.

the sum potential and 3.32% for the difference potential. We also calculated the average relative error, which for the sum potential was 0.32% at short range and 0.49% at long range, while for the difference potential it was 0.04% in the short range and 0.90% in the long range. In Fig. 3, we show two-dimensional contour plots of the fitted OH-He  $A'$  PES for  $r = 0.75 a_0$ ,  $r = 1.8324 a_0$  and  $r = 3.00 a_0$ , while in Fig. 4 the same plots are shown for the fitted  $A''$  PES. For the equilibrium bond length  $r_e = 1.8324 a_0$ , our fit of the 3-dimensional potential is in very close agreement with the PES of Lee et al. [26], as it should, since both PES's were calculated with the same *ab initio* method using the same basis set. The absolute potential energy minimum for  $r = 1.8324 a_0$  is located at  $\theta = 69.2^\circ$ ,  $R = 5.69 a_0$  for  $A'$  symmetry, leading to an interaction energy of  $V_{A'} = -30.0 \text{ cm}^{-1}$ . The minimum values for  $\theta = 0^\circ$  and  $\theta = 180^\circ$  were found at  $R = 6.55 a_0$  and  $R = 6.09$ , giving rise to  $V_{A'/A''} = -27.2 \text{ cm}^{-1}$  and  $V_{A'/A''} = -21.7 \text{ cm}^{-1}$ , respectively. A FORTRAN 77 code to generate the interaction potential  $V(R, \theta, r)$  is made available as an EPAPS document [41].

To use the three dimensional potential for scattering, we started with the three-dimensional AVTZ potential,

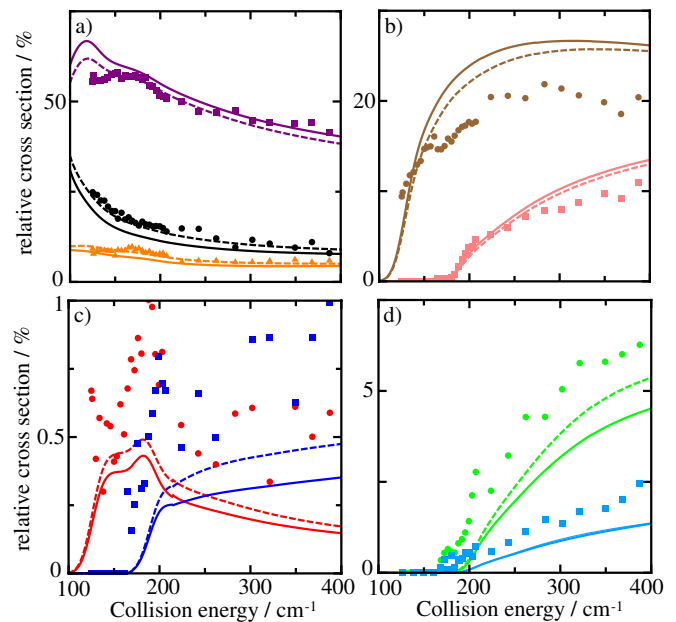


FIG. 5: Relative state-to-state inelastic scattering cross sections of OH ( $X^2\Pi, j = 3/2, F_1, f$ ) radicals with He atoms. The experimental data points from Ref. 34 are shown as dots, while the theoretically calculated cross sections with the potential of Lee et al. [26] are included as solid curves, and the results with the adiabatic potential as dashed curves. On the vertical axes of the plots, 100 % refers to the total inelastic cross section. Relative cross sections for inelastic collisions populating the (a)  $j = 3/2, F_1, e$  (black),  $j = 5/2, F_1, e$  (purple), and  $j = 5/2, F_1, f$  (orange) states; (b) the  $j = 1/2, F_2, e$  (brown) and  $j = 3/2, F_2, f$  (pink) states; (c) the  $j = 1/2, F_2, f$  (red) and  $j = 3/2, F_2, e$  (blue) states; (d) the  $j = 7/2, F_1, e$  (green) and  $j = 7/2, F_1, f$  (cyan) states.

and then subtracted the values of this potential at  $r = r_0$  and added the two-dimensional potential calculated for  $r = r_0$  at the AV5Z level. This implies that the dependence of the intermolecular potential on the most relevant coordinates for the scattering calculation, namely  $R$  and  $\theta$ , is computed at the AV5Z level for  $r = r_0$ , while the variation of the potential with the OH bond length  $r$  is taken into account at the AVTZ level. We solved for the OH vibrational motion in the full 3D potential generated by taking the intermolecular potential energy  $V(R, \theta, r)$  and adding the free OH monomer potential  $V_{\text{OH}}(r)$  [43]. For fixed  $R$  and  $\theta$  this leads to an effectively one-dimensional problem that can be easily solved by standard numerical methods, such as the discrete variable representation based on sinc-functions (sinc-DVR) [44]. Taking the resulting ground state energy for each  $R$  and  $\theta$  and subtracting the  $v = 0$  monomer vibrational energy in the absence of the He atom then results in an adiabatic two-dimensional PES. We found, actually, that this adiabatic potential is very similar to the ‘diabatic’ potential obtained by first calculating the lowest vibrational state of OH in the monomer potential  $V_{\text{OH}}(r)$  and then averaging the interaction potential  $V(R, \theta, r)$  over

this ground state. The two methods are expected to give similar results since the vibrational levels of OH are well separated in energy, so that the weak OH-He interaction gives only a slight admixture of the higher vibrational states of OH.

The inelastic OH-He cross sections with OH initially in the  $j = 3/2, F_1, f$  level were calculated with the adiabatic potential. The results are shown in Fig. 5, where the experimental data of Ref. 34 is also shown, as well as the scattering results obtained with the potential of Lee *et al.* [26]. The theoretical data are convoluted with the experimental energy resolution. To this end a Gaussian energy distribution is taken with a standard deviation that is a function of the energy. The value of the standard deviation ranges from  $24 \text{ cm}^{-1}$  at low collision energies to  $59 \text{ cm}^{-1}$  at the highest collision energies. We note that the relative cross sections are plotted, rather than the absolute cross sections, because these relative cross sections are experimentally measured. More details can be found in Refs. 13, 34. We see from Fig. 5 that the overall the agreement with experimental data has improved noticeably with the adiabatic potential.

#### IV. OH-HELIUM COLLISIONS

##### A. State-to-state integral cross sections

For OH-He collisions, the state-to-state scattering cross sections were calculated with the adiabatic potential described in the previous section. In Fig. 6, the energy dependence of the state-to-state integral cross sections for several transitions out of the  $j = 3/2, F_1, f$  level of OH are shown. This level, which is the higher  $\Lambda$ -doublet component of the ground rotational level (see Fig. 1), can be selected with the Stark decelerator since it is low-field seeking in an inhomogeneous electric field [13]. The cross sections are computed on a very fine grid of energies to be able to study resonant features in detail.

Away from the resonances, these results are in good agreement with those previously reported by Klos *et al.* [21]. As noted by these authors, there is a propensity for transitions preserving the total parity. The cross sections are found to be smaller for transitions with large energy gaps. The initial and final levels of the two transitions shown in Fig. 6(a) have a rather large energy separation ( $> 100 \text{ cm}^{-1}$ ), and the total parity is inverted during the transitions. Hence, the cross sections for these transitions are small.

Resonances can be observed in Fig. 6 near the collision energies corresponding to thresholds for excitation of the OH radical to higher rotational and spin-orbit levels. Both shape resonances, which appear right above the threshold energies for the final levels, and Feshbach resonances, which appear near the energies where higher rotational levels than the considered outgoing channel become open, are present. Except for the  $j = 3/2, F_1, f \rightarrow j = 3/2, F_1, e$  and the  $j = 3/2, F_1, f \rightarrow j = 1/2, F_2, f$

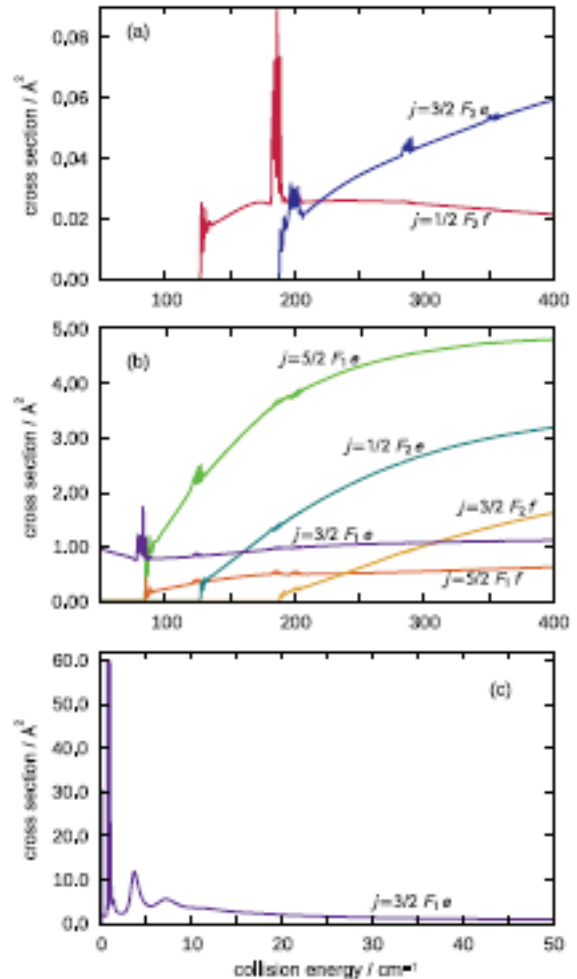


FIG. 6: State-to-state integral cross sections *vs.* collision energy for transitions out of the OH  $j = 3/2, F_1, f$  level in collisions with He. The final levels are indicated for each transition for which the cross section is plotted.

transitions, the Feshbach resonances are not significant compared with the background continuum. The  $j = 3/2, F_1, f \rightarrow j = 3/2, F_1, e$  transition dominates at low collision energies and also gives rise to shape resonances with cross sections peaking above  $10 \text{ \AA}^2$ . However, these shape resonances occur at collision energies of only a few wavenumbers.

In the following subsections, we analyze the shape resonances in the  $j = 3/2, F_1, f \rightarrow j = 5/2, F_1, e$  transition and the Feshbach resonances in the  $j = 3/2, F_1, f \rightarrow j = 1/2, F_2, f$  transition. The former transition has a large cross section; the latter transition exhibits strong resonances that show the largest enhancement compared to the background.

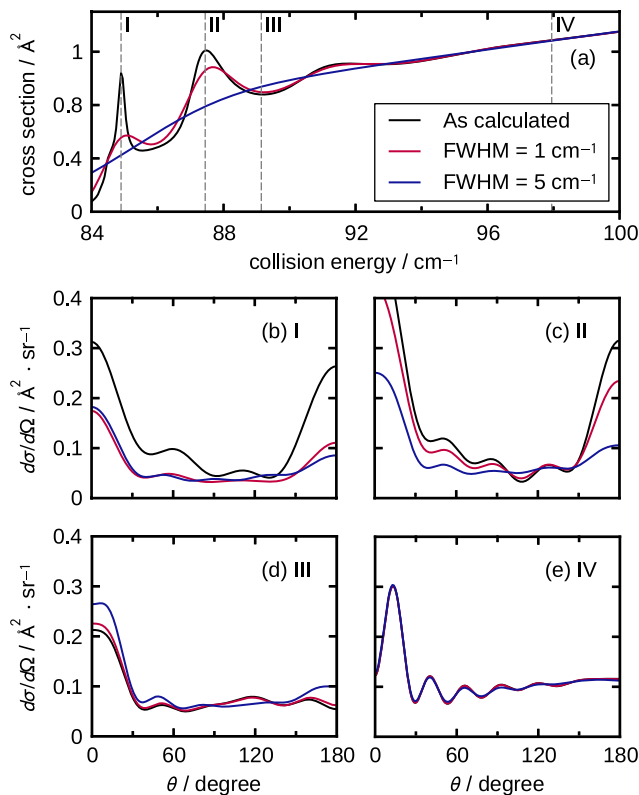


FIG. 7: (a) State-to-state integral cross sections *vs.* collision energy for the  $j = 3/2, F_1, f \rightarrow j = 5/2, F_1, e$  transition of OH in collisions with He (thick line), and the integral cross section convoluted with Gaussian energy distributions of FWHM of 1 and 5  $\text{cm}^{-1}$  (thin lines). (b)–(e) Differential cross sections  $d\sigma/d\Omega$  of the above transition at several energies marked as dashed lines with Roman numerals in (a), together with the differential cross sections convoluted with Gaussian energy distributions as in (a).

## B. Shape resonances

Shape resonances result from quasi-bound states of the van der Waals complex formed by the collision partners at energies just above the threshold for the final level. All integral cross sections plotted in Fig. 6 display shape resonances. In this subsection we analyze the shape resonances associated with the  $j = 3/2, F_1, f \rightarrow j = 5/2, F_1, e$  transition since it has a large integral cross section. Figure 7(a) displays these resonances on an expanded energy scale. Several maxima, with increasing peak width *vs.* energy, can be observed, as was also previously found [24] for OH-He and other He-molecule systems [5, 45, 46].

To gain more insight, we employ the adiabatic bender model [29, 30] to analyze the shape resonances. The method is similar to the previous analysis of OH-He collisions by Dagdigian and Alexander [24], except that we used a close-coupling channel basis instead of a coupled-states one. The full Hamiltonian with the inclusion of Coriolis coupling and only the radial nuclear kinetic en-

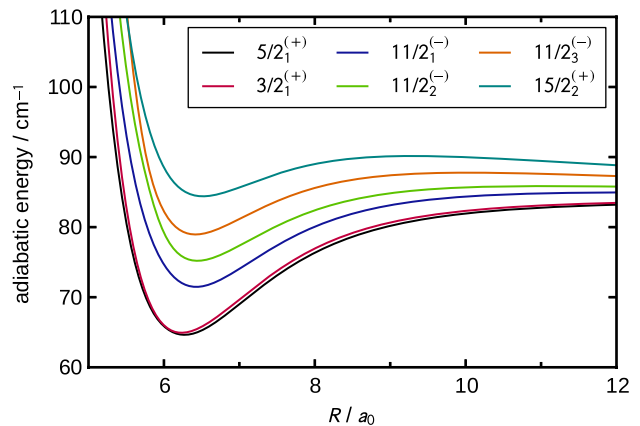


FIG. 8: Plots of the OH-He adiabatic bender curves that correlate with the OH  $j = 5/2, F_1, e$  level, obtained from close-coupling calculations. Curves are labeled with  $J_n^{(p)}$ , where  $J$ ,  $p$ , and  $n$  are the total angular momentum, the total parity of the scattering wavefunction, and the cardinal index, respectively.

ergy excluded is diagonalized as a function of  $R$ . The eigenvalues define a set of adiabatic bender potential energy curves, which are labeled by the total angular momentum  $J$ , the total parity  $p$  of the scattering wavefunction, and the cardinal index  $n$  of the eigenvalue. In this paper, we will use the symbol  $J_n^{(+)}$  and  $J_n^{(-)}$  to label close-coupling adiabatic bender curves with  $p = +1$  and  $p = -1$ , respectively.

Figure 8 shows several adiabatic bender curves that correlate with the OH  $j = 5/2, F_1, e$  level. The curves marked with  $5/2_1^{(+)}$  and  $3/2_1^{(+)}$  are the two lowest lying adiabatic bender curves, each of which supports only one bound stretch level, with energies of  $77.47 \text{ cm}^{-1}$  and  $78.15 \text{ cm}^{-1}$ , respectively. As  $J$  and  $n$  increase, the curves move up in energy and the well depths become smaller. As a consequence, some of the bound levels become quasi-bound, and for the high lying curves (for example, the  $15/2_2^{(+)}$  curve shown in Fig. 8) the wells are too shallow to support any quasi-bound levels.

To compute the energies of the shape resonances, we treat the adiabatic bender curves in conventional one-dimensional scattering problems and calculate the phase shift. We should be able to observe rapid changes by  $\pi$ , signifying resonances, in the collision energy dependence of phase shift [4]. Fig. 9 shows the phase shift as a function of collision energy for all the adiabatic bender curves that have such a feature. We see from Fig. 9 that resonances in six adiabatic bender curves contribute to each of the three peaks shown in Fig. 7(a) (labeled as I, II, and III), which occur at  $84.8, 87.6$  and  $91 \text{ cm}^{-1}$ , respectively. The resonance features in Fig. 7(a) and Fig. 9 match well both in energy and width. Note that in order to distinguish the phase shift in different adiabatic bender curves, Fig. 9(b) and (c) do not show the whole range of the resonances, and thus the resonant changes

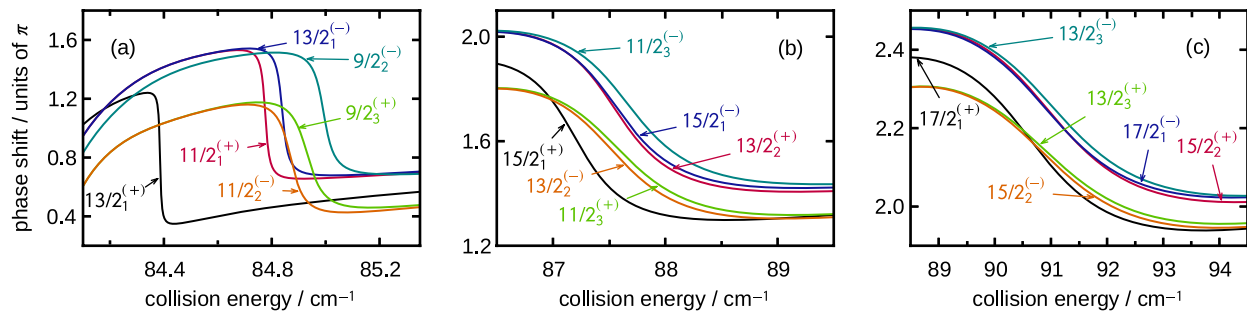


FIG. 9: Phase shifts as a function of collision energy for OH( $j = 5/2, F_1, e$ )-He collisions, obtained from close-coupling adiabatic bender curves described in the text and shown in Fig. 8. Curves are labeled with  $J_n^{(p)}$ , where  $J$ ,  $p$ , and  $n$  are the total angular momentum, the total parity of the scattering wavefunction, and the cardinal index, respectively.

in phase shift shown are less than  $\pi$ .

It is also interesting to compare the differential cross sections for collision energies on and off a resonance. Figures 7(b)–(e) display differential cross section for several energies marked in Fig. 7(a) with Roman numerals. The center of the two major peaks are marked as I and II, while III and IV correspond to non-resonant energies. We observe significant backward scattering for energies I and II, likely because of an increased time delay of collision due to the formation and decay of quasi-bound levels of the van der Waals complex. Backward peaks are insignificant for energies III and IV. We will further discuss this topic in the next subsection.

### C. Feshbach resonances

In Feshbach resonances, quasi-bound levels of the collision complex associated with a given rotational level dissociate to yield the molecule in a lower-energy rotational level. We consider here Feshbach resonances associated with the  $j = 3/2, F_1, f \rightarrow j = 1/2, F_2, f$  transition. This transition was chosen for detailed study since the resonance features show a *ca.* 4-fold increase over the continuum background (see Fig. 6). Figure 10(a) displays these resonances on an expanded energy scale.

It is seen that a rich set of Feshbach resonances exists in a collision energy range of several  $\text{cm}^{-1}$  below the energetic threshold for opening of the  $F_2, j = 3/2$  level at  $188 \text{ cm}^{-1}$ . Figure 11 displays the contribution to the integral cross section for the  $j = 3/2, F_1, f \rightarrow j = 1/2, F_2, f$  transition from various values of the total angular momentum  $J$  (partial cross sections). The individual partial cross sections exhibit one or more peaks, and their energies shift toward higher collision energy as  $J$  increases. For  $J \geq 13/2$ , no significant resonances can be found in the energy dependence of partial cross sections.

We performed an adiabatic bender analysis similar to that described in subsection IV B. We calculated adiabatic bender potentials by diagonalizing the Hamiltonian expressed in a close-coupling channel basis. Since all possible values of  $l$  (the orbital angular momentum of the

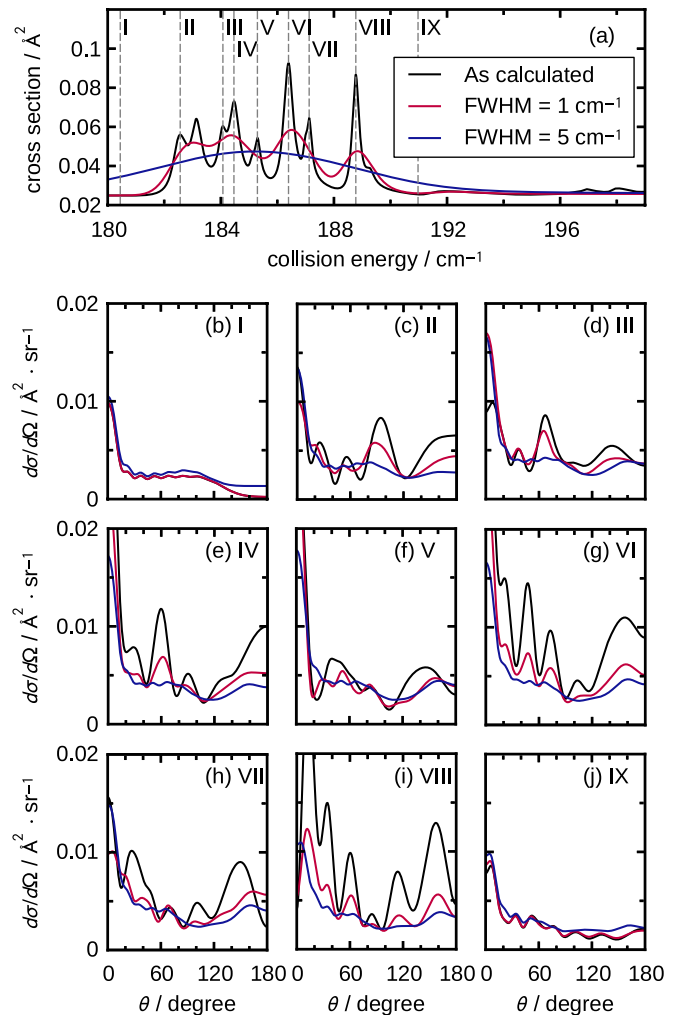


FIG. 10: (a) State-to-state integral cross section *vs.* collision energy for the  $j = 3/2, F_1, f \rightarrow j = 1/2, F_2, f$  transition of OH in collisions with He (black line), and the integral cross section convoluted with Gaussian energy distributions with FWHM of 1 (red line) and  $5 \text{ cm}^{-1}$  (blue line). (b)–(j) Differential cross sections  $d\sigma/d\Omega$  of the above transition at several energies marked as dashed lines and Roman numerals in (a), together with the convoluted differential cross sections with Gaussian energy distribution as in (a).



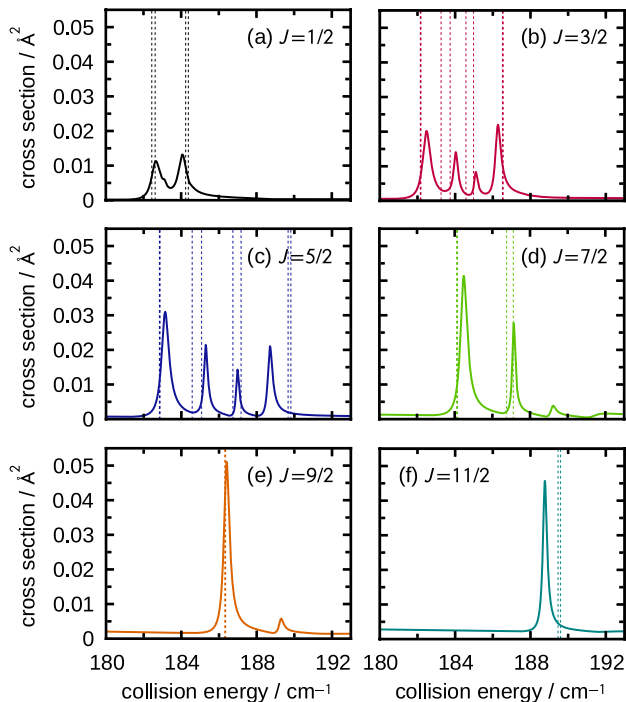


FIG. 11: Partial cross sections *vs.* collision energy for the  $j = 3/2, F_1, f \rightarrow j = 1/2, F_2, f$  transition of OH in collisions with He for total angular momentum  $J \leq 11/2$ . The dotted vertical lines denote the computed energies of the van der Waals stretch levels supported by the close-coupling adiabatic bend curves.

van der Waals complex) are included in the channel basis, there are multiple adiabatic bend curves for each value of  $J$ . These adiabatic bend curves look similar to those shown in Fig. 8 and are not plotted here. The energies of the van der Waals stretch levels supported by these curves were derived using a fixed step-size discrete variable representation (DVR) method[47, 48]. To treat levels that might be quasi-bound, an infinite barrier was placed at the maximum of the centrifugal barrier on each adiabatic bend potential. For curves associated with large  $J$ , this approximation will lead to calculated energies higher than they should be and could lead to significant error. These computed energies are shown as dotted lines in Fig. 11. There is a reasonable match between the energies of the resonances and of the bend-stretch levels, especially for small  $J$ .

Fig. 10(b)–(j) display the differential cross section for the OH  $j = 3/2, F_1, f \rightarrow j = 1/2, F_2, f$  transition at several energies marked on Fig. 10(a) with Roman numerals. The energies at I and IX are not at a resonance, and the differential cross sections show little backward scattering, while II – IV correspond to resonance energies, for which some backward scattering can be observed. The shapes of the differential cross sections are quite different at resonance energies compared to collision energies away from the resonances.

A simple way to analyze the resonances and to quali-

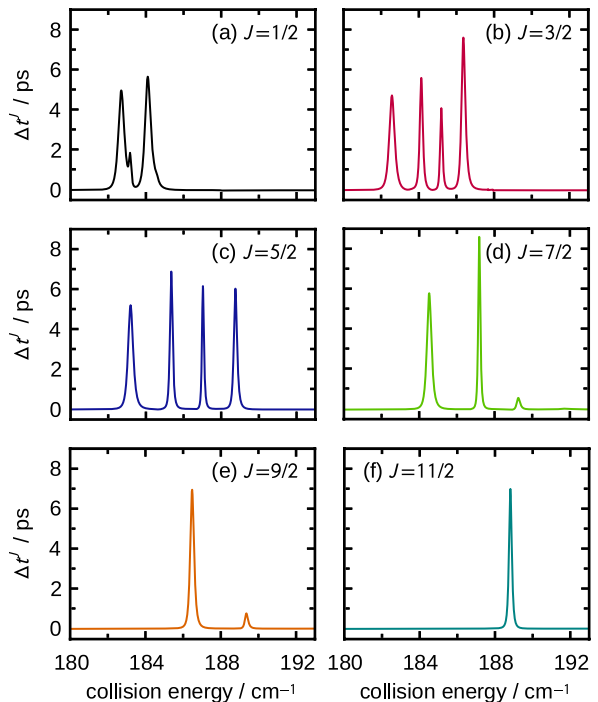


FIG. 12: Collision lifetime  $\Delta t^J(E)$  as a function of collision energy for the OH  $j = 3/2, F_1, f \rightarrow j = 1/2, F_2, f$  transition in collisions with He, as defined in Eq. (9) of the text, for total angular momenta  $J = 1/2 - 11/2$ .

tatively explain backward scattering appearing in differential cross sections is to calculate the collision lifetime, which is the difference between the time that the collision partners spend in each other's neighborhood with and without the interaction [31, 49, 50]. For a direct comparison with the partial cross sections shown in Fig. 11, we compute the collision lifetime from initial state  $\gamma$  to final state  $\gamma'$  for individual total angular momenta  $J$ , defined as

$$\Delta t_{\gamma\gamma'}^J(E) = \text{Re} \left[ -i\hbar \sum_{l,p,l',p'} \delta_{pp'} (S_{\gamma,\gamma',l,l'}^J)^* \frac{dS_{\gamma,\gamma',l,l'}^J}{dE} \right] \quad (9)$$

where  $l, p$  and  $l', p'$  denotes the orbital angular momentum and parity of initial and final levels, respectively, and  $S_{\gamma,\gamma',l,l'}^J$  denotes  $S$ -matrix elements for total angular momentum  $J$  from close-coupling calculations. The lifetimes *vs.*  $J$  for the  $j = 3/2, F_1, f \rightarrow j = 1/2, F_2, f$  transition are plotted in Fig. 12. Clearly, the resonance peaks in Fig. 11 are well reproduced, with collision lifetimes of a few picoseconds. The most intense resonance peak lies at  $186.4 \text{ cm}^{-1}$ , which was largely due to the  $J = 9/2$  partial cross section. From Fig. 12 we see that the corresponding lifetime is about 6 ps. We can compare this collision lifetime with the rotational period of the OH-He van der Waals complex. We estimate the rotational constant of the complex to be  $6.4 \times 10^{-24} \text{ J}$  from the expectation value of  $1/R^2$  computed with the wave

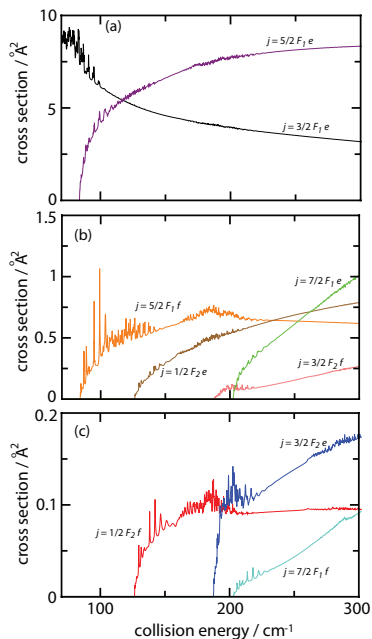


FIG. 13: State-to-state inelastic scattering cross sections of OH ( $X^2\Pi_{3/2}, j = 3/2, f$ ) radicals with Ne atoms as a function of the collision energy. Cross sections for inelastic collisions populating the (a)  $j = 3/2, F_1, e$  (black) and the  $j = 5/2, F_1, e$  (purple) states; (b) the  $j = 5/2, F_1, f$  (orange),  $j = 1/2, F_2, e$  (brown),  $j = 3/2, F_2, f$  (pink), and the  $j = 7/2, F_1, e$  (green) states; (c) the  $j = 1/2, F_2, f$  (red),  $j = 3/2, F_2, e$  (blue), and the  $j = 7/2, F_1, f$  (cyan) states.

function obtained from the DVR method on the lowest lying  $J = 9/2$  adiabatic bender curve. This corresponds to a rotational period 14.9 ps, assuming  $l = 3$ .

We thus conclude that the collision lifetime has the same order of magnitude as the rotational period of the OH-He complex. It is therefore not surprising to observe significant backward scattering at some resonance energies. At off-resonance energies the collision lifetime will be  $\ll 1$  ps, which is much smaller than the OH-He rotational period. Hence, backward scattering is expected to be barely observable.

## V. OH-NEON COLLISIONS

To describe the interaction between OH and Ne, we used the PES of Sumiyoshi et al. [32]. This PES was calculated using an explicitly correlated, spin-unrestricted coupled-cluster approach [UCCSD(T)-F12b] with a quintuple-zeta basis set (AV5Z). Although Sumiyoshi et al. calculated a three-dimensional potential, we used in Ref. [34] their interaction potential evaluated at the equilibrium distance  $r_e = 1.832 a_0$  for the scattering calculations, so that no effect of the OH vi-

brational motion was included. In that reference it was shown that this procedure already gives excellent agreement between theory and high-precision scattering experiments for OH-Ne collisions. Since we found in Section III that the vibrational motion of OH can be of quantitative influence, we also calculated an adiabatic potential from the three-dimensional potential of Sumiyoshi et al. in the same way as we did for OH-He. The resulting adiabatic potential was found to improve slightly the excellent agreement with the experimental results for the scattering of OH and Ne. In the present study, we use the adiabatic potential throughout and compute the cross sections on a much finer grid than in the study by Scharfenberg et al. [34] in order to study scattering resonances. In Fig. 13 we show the energy dependence of state-to-state integral cross sections for collisions of the OH radical with Ne atoms, where the OH radicals are initially in the  $j = 3/2, F_1, f$  level. Overall, the behavior of the inelastic cross sections as a function of energy is rather similar to what was observed for the OH-He system in Section IV. For example, we again observe a propensity for transitions preserving the total parity. However, in the OH-Ne system none of the channels appears to have particularly strong Feshbach resonances, as was the case for the  $j = 3/2, F_1, f \rightarrow j = 1/2, F_2, f$  transition of the OH-He system. The most pronounced resonant features observed for OH-Ne collisions are shape resonances in the  $j = 3/2, F_1, f \rightarrow j = 5/2, F_1, f$  transition. In Fig. 14 we show these shape resonances in more detail.

Looking closely at Fig. 14, we see several resonance peaks that correspond to an increase in the cross section by about a factor of two compared to the nonresonant energies. A relatively strong resonance occurs at a collision energy of  $99.23 \text{ cm}^{-1}$ ; this resonance increases the cross section by a factor of four compared to the background. The latter resonance is indicated by the Roman numeral V. The main contributions to this resonance originate from partial cross sections with total angular momenta of  $J = 37/2$  and  $J = 39/2$ . In Fig. 14, we also show the differential cross sections for several energies that are marked by Roman numerals in panel (a). For the resonances at collision energies of 86.83, 94.90 and  $99.23 \text{ cm}^{-1}$ , the cross sections are shown in the panels (b), (d) and (f). In these plots, large amplitudes for backscattering are observed. To compare, the differential cross sections were also calculated away from the resonances at the energies 93.00, 98.00 and  $101.00 \text{ cm}^{-1}$ , and the results are shown in the panels (c), (e) and (g). In the case of nonresonant scattering, the observed backscattering is significantly reduced. The differential cross sections at these resonances look similar to those at the shape resonances for the  $j = 3/2, F_1, f \rightarrow j = 5/2, F_1, e$  transition of the OH-He system (see Fig. 7), where also an increase in backscattering was found. With a measurement of the differential cross sections, the strong increase and decrease in the backscattering might help in experimentally identifying the shape resonances at 94.90 and  $99.23$

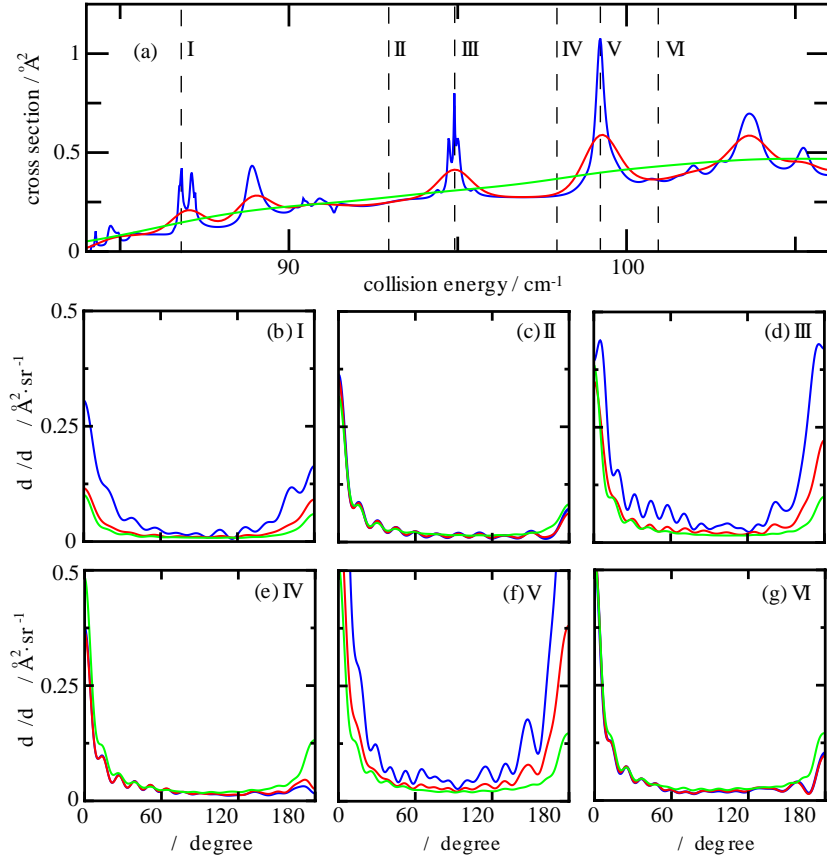


FIG. 14: (a) Integral cross section for collisions of OH radicals with Ne atoms as a function of the collision energy. The initial state of the OH radical is the  $j = 3/2, F_1, f$  state and the final state is the  $j = 5/2, F_1, f$  state. The blue curve shows the theoretical results without any convolution, the red curve shows the integral cross section convoluted with a Gaussian energy distribution having a FWHM of  $1 \text{ cm}^{-1}$ , while for the green curve a FWHM of  $5 \text{ cm}^{-1}$  was used. At the collision energies designated with the Roman numerals I-VI, differential cross sections were calculated, shown in panels (b) to (g). Again the blue curves are not convoluted, while for the red curves a FWHM of  $1 \text{ cm}^{-1}$  was used, and for the green curves a FWHM of  $5 \text{ cm}^{-1}$ . At the scattering resonances (I, III and V), strong backscattering is observed.

$\text{cm}^{-1}$ . However, we note that one must be careful with identifying the backscattering signal with resonances in the cross section. Namely, in Fig. 14(a) also less pronounced resonances are seen, and not all of them have such a strong backscattering signal as the strongest resonances I, III and V. Moreover, closer to the threshold of the  $j = 3/2, F_1, f \rightarrow j = 5/2, F_1, e$  transition significant backscattering is observed away from the resonances.

## VI. DISCUSSION

The experimental observation of resonance structures as discussed in this paper would comprise a very detailed test for the calculated PES's and scattering calculations on these PES's. The Stark deceleration technique provides a source of state-selected molecules with a tunable velocity and narrow velocity distribution. This technique enables state-to-state scattering experiments in which the collision energy can be precisely tuned over a wide range with a high collision energy resolution. Yet, the obser-

vation of scattering resonances requires an energy resolution that has not yet been achieved in this type of experiments. In this section, we analyze the collision energy resolution required to observe resonance features in either the state-to-state integral or the differential cross sections for OH-He and OH-Ne collisions. We discuss the requirements on the beam velocity and angular distributions, and discuss the feasibility of obtaining these distributions.

Referring back to Figs. 7, 10, and 14, the most prominent resonance structures are found for OH-He in the  $j = 3/2, F_1, f \rightarrow j = 3/2, F_1, e$ ,  $j = 3/2, F_1, f \rightarrow j = 5/2, F_1, e$  and the  $j = 3/2, F_1, f \rightarrow j = 5/2, F_2, f$  transitions. For OH-Ne collisions the  $j = 3/2, F_1, f \rightarrow j = 5/2, F_1, f$  channel is of most relevance. To simulate what would be observed in a molecular beam scattering experiment, the integral cross sections in Figs. 7, 10, and 14 are convoluted with Gaussian collision energy distributions of  $1$  and  $5 \text{ cm}^{-1}$  full width at half maximum (FWHM). In Fig. 15, the resonance structure at collision energies around  $85 \text{ cm}^{-1}$  for the  $j = 3/2, F_1, f \rightarrow$

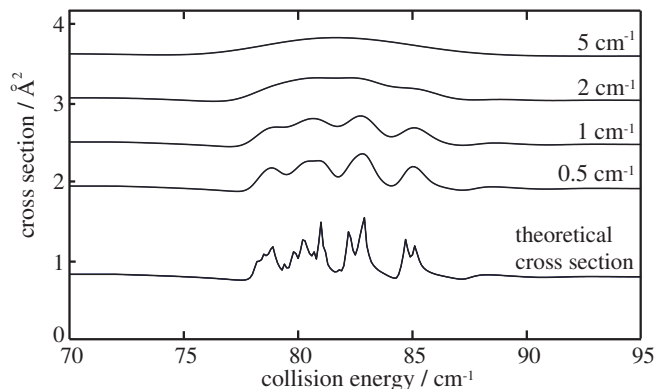


FIG. 15: Inelastic scattering cross section for the  $j = 3/2, F_1, f \rightarrow j = 3/2, F_1, e$  channel in collisions of OH radicals with He atoms, showing Feshbach resonances that correspond to the opening of the  $j = 5/2, F_1$  rotational levels of OH. The theoretical curve is convoluted with Gaussian energy distributions with FWHM of  $0.5 \text{ cm}^{-1}$ ,  $1 \text{ cm}^{-1}$ ,  $2 \text{ cm}^{-1}$ , and  $5 \text{ cm}^{-1}$ . The upper four curves have been given a vertical offset for reasons of clarity.

$j = 3/2, F_1, e$  channel in OH-He collisions is shown. This scattering channel displays a number of Feshbach resonances, corresponding to the opening of the  $j = 5/2, F_1$  channels, that are grouped within a relatively narrow range of collision energies. The theoretical curve is convoluted using  $0.5, 1, 2,$  and  $5 \text{ cm}^{-1}$  (FWHM) energy distributions. We will use this scattering channel as a benchmark to establish the energy resolution required in the experiments to observe signatures of scattering resonances. Scattering resonances are partially resolved for energy resolutions of  $\leq 1 \text{ cm}^{-1}$ . When a resolution between 1 and  $2 \text{ cm}^{-1}$  is achieved, some of the resonance structure is resolved, while for resolutions of  $5 \text{ cm}^{-1}$ , most of the resonance structure has disappeared. In these cases, at best only a broad peak is observed in the integral cross section.

For given beam velocity and angular spread, the collision energy distribution is a function of the collision energy; the highest resolutions are obtained for the lowest collision energies. We can estimate the beam parameters required to reach collision energy distributions of  $\leq 2 \text{ cm}^{-1}$  at a collision energy of  $85 \text{ cm}^{-1}$  for collisions of Stark-decelerated OH radicals with He atoms, i.e., to (partially) resolve the scattering resonances shown in Fig. 15. We assume a beam intersection angle of  $45^\circ$  and choose the velocities of the He and OH beams such that the relative velocity vector is perpendicular to the He atom velocity vector. In this geometry, the collision energy distribution is almost independent of the He atom beam velocity spread [16]. A collision energy of  $85 \text{ cm}^{-1}$  is reached for He and OH velocities of  $790 \text{ m/s}$  and  $1120 \text{ m/s}$ , respectively. In the chosen geometry, the most critical parameter that determines the collision energy resolution is the distribution in beam intersection angles  $\Delta\phi$ . If we assume extremely well collimated beams

such that  $\Delta\phi = 10 \text{ mrad}$  (corresponding to  $0.6^\circ$ ), a velocity spread of the OH radicals of  $5 \text{ m/s}$  results in a collision energy resolution of  $1.9 \text{ cm}^{-1}$ .

Experimentally, the most challenging requirement is the angular spread of both beams. Multiple collimation slits for both the OH and He beams are required to reach the required angular spreads. The required He atom velocity can be obtained using a cryogenic source that is maintained at a temperature of  $60 \text{ K}$ , and the required OH velocity can be produced using the Stark decelerator. The required velocity spread for the OH radicals can be obtained using the Stark decelerator, either by choosing the appropriate phase angle in the decelerator [51], or by additional phase-space manipulation techniques [52]. For the OH-Ne system, even more stringent requirements apply to the beam distributions due to the higher reduced mass for this system. Beam speeds of  $664 \text{ m/s}$  and  $470 \text{ m/s}$  for the OH radical beam and Ne atom, respectively, will result in a collision energy of  $85 \text{ cm}^{-1}$  using a beam crossing angle of  $45^\circ$ . For the velocity and angular distributions used above for OH-He, a collision energy distribution of  $2.1 \text{ cm}^{-1}$  is obtained.

The signatures of scattering resonances can also be inferred from differential cross sections. State-to-state differential cross sections can be measured using the velocity map imaging technique, that provides the full angular and velocity distribution of the scattered molecules [53]. Alternatively, information on the differential cross section may be obtained via Doppler profile measurements of the scattered molecules. The backward scattered components that appear in the differential cross sections when a resonance is accessed offers interesting prospects to reveal the existence of resonances. As the collision energy is tuned over a group of scattering resonances, the presence of these resonances can in principle be inferred from the measured product flux at backward scattering angles. In Figs. 7, 10, and 14, the differential cross sections are shown at collision energies near and at the resonances, convoluted with Gaussian collision energy distributions of  $1$  and  $5 \text{ cm}^{-1}$  full width at half maximum (FWHM). In particular for the  $j = 3/2, F_1, f \rightarrow j = 5/2, F_1, f$  channel in OH-Ne, a significant scattering intensity at backward scattering angles remains, even for a collision energy resolution as high as  $5 \text{ cm}^{-1}$ . In the integral cross section, no signature of the scattering resonances is observable at these energy resolutions. In these cases, it may be favorable to experimentally explore the existence of resonances via measurements of differential cross sections instead of integral cross sections.

The examples treated above show that collision energy resolutions in the  $1 - 2 \text{ cm}^{-1}$  range, although very challenging experimentally, should allow for the observation of both shape and Feshbach resonances in the integral cross sections for inelastic collisions between OH radicals and He or Ne atoms. The OH radical is an excellent candidate in these experiments, as a sensitive detection scheme, appropriate for ion imaging, has recently been



developed for this species [54]. In addition, the relatively large rotational spacing of the molecular levels results in a molecular beam pulse with less initial population in excited rotational states, and therefore a packet of Stark-decelerated OH radicals with a high state purity. This facilitates the sensitive and background free detection of scattering products and enables the implementation of beam collimators that improve the angular and velocity spreads of the beams at the cost of particle densities. The disadvantage of the large rotational spacing, however, is the relatively high energies of the energetic thresholds for inelastic scattering, and corresponding relatively high collision energies at which scattering resonances appear. In this respect, the inelastic scattering of OD radicals or ND<sub>3</sub> molecules with He and Ne atoms will be interesting candidates for studying scattering resonances as well, reducing the energy for the lowest lying threshold to 42 cm<sup>-1</sup> and 14 cm<sup>-1</sup>, respectively. To reach a collision energy resolution  $\leq 2$  cm<sup>-1</sup> at these energies will relax the requirements on the velocity and angular spreads of both beams. We will investigate resonance effects in the rotationally inelastic scattering of OD and ammonia molecules with He atoms in forthcoming publications.

## VII. CONCLUSIONS

We have presented detailed calculations on scattering resonances in the rotationally inelastic scattering of OH radicals with He and Ne atoms. For OH-He, we have developed new 3D *ab initio* potential energy surfaces, and the inelastic scattering cross sections that are derived from these surfaces compare favorably with recent experiments. We have identified numerous scattering resonances – of both the shape and Feshbach types – in the integral cross sections. We have analyzed these resonances using the adiabatic bender model and computed collision lifetimes. We observe dramatic changes in the differen-

tial cross sections at the resonances, showing in selected cases a forward-backward peaking of the scattered flux. The analysis of scattering resonances presented here will be indispensable in the experimental search for such resonances in, for instance, crossed beam scattering experiments using Stark-decelerated molecular beams. To experimentally observe signatures of resonances in the integral cross sections and to partially resolve individual resonances, a collision energy resolution of  $\leq 2$  cm<sup>-1</sup> is required. Obtaining energy resolutions  $\leq 2$  cm<sup>-1</sup> mainly requires highly collimated molecular beams, which appears challenging. Alternatively, signatures of scattering resonances may be found in the differential cross sections. The selective detection of scattered molecules at backward scattering angles may facilitate the identification of resonances if the collision energy resolution is not sufficient to resolve them in the integral cross sections.

## ACKNOWLEDGMENTS

KBG acknowledges support by the European Community's Seventh Framework Program ERC-2009-AdG under grant agreement 247142-MolChip. MHA gratefully acknowledges financial support from the US National Science Foundation under grant No. CHE-0848110. AvdA thanks the Alexander von Humboldt foundation for a Humboldt Research Award. SYTM acknowledges financial support from Netherlands Organisation for Scientific Research (NWO) via a VIDI grant. We thank our colleagues from the Fritz-Haber-Institut in Berlin for fruitful discussions. In particular, we thank Moritz Kirste for providing the data of Figure 5, and Christian Schewe for help in preparing Figure 15 and discussions on the feasibility of experimentally observing resonances using Stark-decelerated beams of OH. We thank Gerard Meijer for carefully reading the manuscript, and for general support.

- 
- [1] R. B. Bernstein, ed., *Atom-Molecule Collision Theory: A Guide for the Experimentalist* (Plenum Press, New York, 1979).
  - [2] Z. Bačić and R. E. Miller, *J. Phys. Chem.* **100**, 12945 (1996).
  - [3] P. E. S. Wormer and A. van der Avoird, *Chem. Reviews* **100**, 4109 (2000).
  - [4] M. S. Child, *Molecular Collision Theory* (Academic Press, London and New York, 1974).
  - [5] F. Lique, G. Li, H.-J. Werner, and M. H. Alexander, *J. Chem. Phys.* **134**, 231101 (2011).
  - [6] D. W. Chandler, *J. Comp. Phys.* **132**, 110901 (2010).
  - [7] A. Schutte, D. Bassi, F. Tommasini, and G. Scoles, *Phys. Rev. Lett.* **29**, 979 (1975).
  - [8] A. Schutte, D. Bassi, F. Tommasini, and G. Scoles, *J. Chem. Phys.* **62**, 600 (1975).
  - [9] J. P. Toennies, W. Welz, and G. Wolf, *J. Chem. Phys.* **71**, 614 (1979).
  - [10] M. H. Qiu, Z. F. Ren, L. Che, D. X. Dai, S. A. Harich, X. Y. Wang, X. M. Yang, C. X. Xu, D. Q. Xie, M. Gustafsson, et al., *Science* **311**, 1440 (2006).
  - [11] R. B. Bernstein, ed., *Molecular Reaction Dynamics and Chemical Reactivity* (Oxford University Press, New York, 1979).
  - [12] S. Y. T. van de Meerakker, H. L. Bethlem, and G. Meijer, *Nat. Phys.* **4**, 595 (2008).
  - [13] L. Scharfenberg, J. Klos, P. J. Dagdigian, M. H. Alexander, G. Meijer, and S. Y. T. van de Meerakker, *Phys. Chem. Chem. Phys.* **12**, 10660 (2010).
  - [14] J. J. Gilijamse, S. Hoekstra, S. Y. T. van de Meerakker, G. C. Groenenboom, and G. Meijer, *Science* **313**, 1617 (2006).
  - [15] M. Kirste, L. Scharfenberg, J. Klos, F. Lique, M. H. Alexander, G. Meijer, and S. Y. T. van de Meerakker, *Phys. Rev. A* **82**, 042717 (2010).
  - [16] L. Scharfenberg, S. Y. T. van de Meerakker, and G. Mei-

- jer, *Phys. Chem. Chem. Phys.* **13**, 8448 (2011).
- [17] W. Erlewein, M. von Seggeren, and J. P. Toennies, *Zeitschrift für Physik* **211**, 35 (1968).
- [18] M. von Seggeren and J. P. Toennies, *Zeitschrift für Physik* **218**, 341 (1969).
- [19] M. C. van Beek, J. J. ter Meulen, and M. H. Alexander, *J. Chem. Phys.* **113**, 628 (2000).
- [20] M. C. van Beek, J. J. ter Meulen, and M. H. Alexander, *J. Chem. Phys.* **113**, 637 (2000).
- [21] J. Klos, F. Lique, and M. H. Alexander, *Chem. Phys. Lett.* **445**, 12 (2007).
- [22] Z. Pavlovic, T. V. Tscherbul, H. R. Sadeghpour, G. C. Groenenboom, and A. Dalgarno, *J. Phys. Chem. A* **113**, 14670 (2009).
- [23] P. J. Dagdigian and M. H. Alexander, *J. Chem. Phys.* **130**, 094303 (2009).
- [24] P. J. Dagdigian and M. H. Alexander, *J. Chem. Phys.* **130**, 164315 (2009).
- [25] M. H. Alexander, *Chem. Phys.* **92**, 337 (1985).
- [26] H. S. Lee, A. B. McCoy, R. R. Toczyłowski, and S. M. Cybulski, *J. Chem. Phys.* **113**, 5736 (2000).
- [27] J. Han and M. C. Heaven, *J. Chem. Phys.* **123**, 064307 (2005).
- [28] We note that parts of the resonance structure as shown in Fig. 9 of Reference [16] are unfortunately artifacts of the scattering calculation procedure. The conclusion in this paper that resonances may be observed in the experiment if collision energy distributions of  $5 \text{ cm}^{-1}$  are achieved, is unfortunately invalid.
- [29] S. L. Holmgren, M. Waldman, and W. Klemperer, *J. Chem. Phys.* **67**, 4414 (1977).
- [30] M. H. Alexander, S. Gregurick, P. J. Dagdigian, G. W. Lemire, M. J. McQuaid, and R. C. Sausa, *J. Chem. Phys.* **101**, 4547 (1994).
- [31] F. T. Smith, *Phys. Rev.* **118**, 349 (1960).
- [32] Y. Sumiyoshi, I. Funahara, K. Sato, Y. Ohshima, and Y. Endo, *Phys. Chem. Chem. Phys.* **12**, 8340 (2010).
- [33] HIBRIDON is a package of programs for the time-independent quantum treatment of inelastic collisions and photodissociation written by M. H. Alexander, D. E. Manolopoulos, H.-J. Werner, and B. Follmeg, with contributions by P. F. Vohralik, D. Lemoine, G. Corey, R. Gordon, B. Johnson, T. Orlikowski, A. Berning, A. Degli-Esposti, C. Rist, P. J. Dagdigian, B. Pouilly, G. van der Sanden, M. Yang, F. de Weerd, S. Gregurick, F. Lique, and J. Klos. More information and/or a copy of the code can be obtained from the website <http://www2.chem.umd.edu/groups/physical/hibridon/hib43>.
- [34] L. Scharfenberg, K. B. Gubbels, M. Kirste, G. C. Groenenboom, A. van der Avoird, G. Meijer, and S. Y. T. van de Meerakker, *Eur. Phys. J. D* **65**, 189 (2011).
- [35] MOLPRO, version 2008.1, a package of *ab initio* programs, H.-J. Werner, P. J. Knowles, R. Lindh, F. R. Manby, M. Schütz, and others, see <http://www.molpro.net>.
- [36] H. Koch, B. Fernández, and O. Christiansen, *J. Chem. Phys.* **108**, 2784 (1998).
- [37] S. F. Boys and F. Bernardi, *Mol. Phys.* **19**, 553 (1970).
- [38] A. van der Avoird, P. E. S. Wormer, F. Mulder, and R. M. Berns, *Top. Curr. Chem.* **93**, 1 (1980).
- [39] K. T. Tang and J. P. Toennies, *J. Chem. Phys.* **80**, 3726 (1984).
- [40] T.-S. Ho and H. Rabitz, *J. Chem. Phys.* **104**, 2584 (1996).
- [41] See supplementary material at [URL will be inserted by AIP] for the fits of the potential energy surfaces.
- [42] G. C. Groenenboom and N. Balakrishnan, *J. Chem. Phys.* **118**, 7380 (2003).
- [43] M. P. J. van der Loo and G. C. Groenenboom, *J. Chem. Phys.* **126**, 114314 (2007).
- [44] G. C. Groenenboom and D. T. Colbert, *J. Chem. Phys.* **99**, 9681 (1993).
- [45] P. J. Dagdigian and M. H. Alexander, *Mol. Phys.* **108**, 1159 (2010).
- [46] P. J. Dagdigian and M. H. Alexander, *J. Chem. Phys.* **135**, 064306 (2011).
- [47] D. T. Colbert and W. H. Miller, *J. Chem. Phys.* **96**, 1982 (1992).
- [48] L. Tao and M. H. Alexander, *J. Chem. Phys.* **127**, 114301 (2007).
- [49] E. P. Wigner, *Phys. Rev.* **98**, 145 (1955).
- [50] J. F. Castillo, D. E. Manolopoulos, K. Stark, and H.-J. Werner, *J. Chem. Phys.* **104**, 6531 (1996).
- [51] S. Y. T. van de Meerakker, H. L. Bethlem, and G. Meijer, *Nature Physics* **4**, 595 (2008).
- [52] F. M. H. Crompvoets, R. T. Jongma, H. L. Bethlem, A. J. A. van Rooij, and G. Meijer, *Phys. Rev. Lett.* **89**, 093004 (2002).
- [53] It is noted that the resonances appear at low collision energies compared to the energetic threshold of the inelastic channel, rendering the size of the images small. A velocity map imaging detector with zoom lens capability, and ionization schemes that limit the ion recoil in the laser ionization step, will be required to measure these small images.
- [54] J. M. Beames, F. Liu, M. I. Lester, and C. Murray, *J. Chem. Phys.* **134**, 241102 (2011).